Pure and Applied Geophysics

P-SH Conversions in Layered Media with Hexagonally Symmetric Anisotropy: A CookBook

VADIM LEVIN[1] and JEFFREY PARK[1]

Abstract—Reflectivity synthetic seismograms demonstrate that the type, layering and orientation of 1-D anisotropy influences strongly the coda of teleseismic P waves at periods $T > 1$ sec, particularly *P-SH* converted waves. We assume the simplest form of anisotropy described by an elastic tensor with a symmetry axis $\hat{\mathbf{w}}$ of arbitrary orientation. The resulting phase velocities vary as $\cos 2\xi$ with respect to that axis. Using three families of simple crustal models, we compare the effects of an anisotropic surface layer with reverberations caused by both "thick" and "thin" layers of anisotropy at depth. If anisotropy in the surface layer is significant, the polarization of direct P can be distorted to generate a transverse component, followed by Ps and a prominent shear reverberation converted from direct P at the free surface. If the anisotropic layer is buried, the first, and often the most prominent, arrival on the transverse component is the *P-to-SH* conversion at its upper surface. If the anisotropic layer is sufficiently thin, *P-to-SH* conversions from its boundaries interfere to form a derivative pulse shape on the transverse component, which could be mistaken as the signature of shear-wave splitting. If $\hat{\mathbf{w}}$ is horizontal, compressional (P) and shear (S) anisotropy both produce similar waveform perturbations with four-lobed azimuthal patterns, suggesting that a weighted stack of P coda from different back-azimuths would improve signal-to-noise. For $\hat{\mathbf{w}}$ tilted between the horizontal and vertical, however, the effects of P- and S-anisotropy differ greatly. The influence of P-anisotropy on *P-to-S* conversion is greatest for a symmetry axis tilted at 45° to the vertical, where its azimuthal pattern has two lobes, rather than four. Combinations of P- and S-anisotropy typically lead to a composite azimuthal dependence in the P-coda reverberations.

Key words: Seismic anisotropy, crustal structure, body waves, layered media, scattered waves, synthetic seismograms.

Introduction

There is a mounting body of evidence suggesting that seismic isotropy—an important and common assumption in seismological studies—may actually be a rarity rather than the rule in the shallow earth. The majority of minerals and rocks that form the crust and upper mantle display seismic anisotropy in laboratory measurements (BABUSKA and CARA, 1991). Bulk anisotropy in the oceanic crust and lithosphere was established by marine refraction experiments over two decades ago (e.g., RAITT *et al.*, 1969). Shear-wave splitting in broad-band seismic data suggests that the continental lithosphere has significant elastic anisotropy (e.g.,

[1] Department of Geology and Geophysics, Yale University, PO Box 208109, New Haven, CT 06520-8109, U.S.A.

VINNIK et al., 1992; SILVER, 1996; BABUSKA et al., 1993; HEARN, 1996; LEVIN et al., 1996), which can be used to reconstruct both active and fossil bulk strain. The upper part of the continental crust appears to have particularly strong anisotropic properties (ZHI et al., 1994; LYNN, 1991).

The variety of mechanisms producing seismic anisotropy in the crust centers on a handful of scenarios. In the upper crust the strongest influence is believed to be that of aligned cracks and/or pore spaces (BABUSKA and PROS, 1984), for which slower velocities are found for waves that propagate normal to the average crack plane. The aspect ratio of pore/cracks and presence of fluid in them determine the extent and proportion of anisotropy (HUDSON, 1981; CRAMPIN, 1984, 1991). Alternating thin isotropic layers of higher and lower velocity can also produce an overall anisotropic effect (BACKUS, 1962; HELBIG, 1994), with the velocities slower normal to bedding than along it. In the lower crust and the uppermost mantle, cracks are assumed to close in response to increasing overburden pressure (BABUSKA and PROS, 1984; KERN et al., 1993), though field exposures of (formerly) deep-crustal fluid-filled cracks can be found (AGUE, 1995). In the absence of cracks and inclusions, the lattice-preferred orientation (LPO) of mineral crystals is taken as the main cause of seismic anisotropy. Most minerals composing the bulk of the crust are anisotropic to some degree (BABUSKA and CARA, 1991), while properties of olivine and, to a lesser extent, orthopyroxene dominate the upper mantle anisotropy. Different deformation mechanisms can lead to the alignment of either the slow or the fast crystallographic direction in olivine grains (NICOLAS et al., 1973; RIBE, 1992), but LPO caused by dislocation creep in the shallow mantle is commonly believed to lead to preferred alignment of the fast axis (ZHANG and KARATO, 1995). GAHERTY and JORDAN (1995) argue, on the basis of mantle shear-wave reverberations, that thin-layering of different rock types also plays a role in the bulk anisotropy of the continental upper mantle.

Although minerals often exhibit more complex behavior, many instances of seismic anisotropy in crystalline basement rocks display hexagonal symmetry to the first order (e.g., MAINPRICE and SILVER, 1993; BURLINI and FOUNTAIN, 1993). There is no simple relationship between the amount of P velocity anisotropy and that of S anisotropy, but it is rare for only one type, P or S, to be present in a rock. Anisotropy in velocity up to 10% is a common feature of crustal and upper mantle rocks, and exceeds 15% in some lithologies, e.g. metapelites (BURLINI and FOUN-TAIN, 1993). To influence a teleseismic wave in the frequency range 0.2–2 Hz, crack and/or mineral alignment must be coherent within substantial volumes of crust, so the effective anisotropy is often diminished substantially relative to the anisotropy of either minerals and rock samples.

A common assumption in anisotropy studies is that the symmetry axis is either vertical (i.e., as in the case of alternating layers) or horizontal (as in cases of stress-aligned olivine or vertical cracks). On the other hand, a number of studies indicate that an axis with a tilted orientation is needed to explain observations of

teleseismic waves (BABUSKA *et al.*, 1993; LEVIN *et al.*, 1996; GRESILLAUD and CARA, 1996). The possible causes of tilted-axis anisotropy are not exceptional, though one expects only local or regional coherence in the associated details of tectonic deformation. BLACKMAN *et al.* (1996) have modeled tilted alignment of olivine LPO beneath mid-ocean ridge systems. Crustal overthrusting is another likely cause of tilted-axis anisotropy.

Anisotropy induces compressional waves to convert to *SH*-type motion in 1-D velocity structures with horizontal interfaces. KOSAREV *et al.* (1984) and VINNIK and MONTAGNER (1996) invoke this mechanism to explain long-period *SH* phases following teleseismic *P* waves as *P-SH* conversions in horizontally stratified anisotropic upper mantle. *P-SH* conversion resulting from reverberations of a plane wave in a stack of flat anisotropic layers can give rise to *P* coda whose complexity approaches that of observations (LEVIN and PARK, 1997b). Before *P-SH* conversions can be useful in studies of crustal structure, certain questions about the effects of the anisotropic layered medium should be addressed. We need to know which of the possible converted phases will have sufficient energy to be observable in real data. Of these, we must identify phases that may be used to distinguish various types of anisotropic structures, i.e., *P* vs *S* anisotropy, fast versus slow velocity alignment. We also must determine which portions of a layered structure are most promising in terms of generating large *P-SH* phases. Back-azimuth dependence unique to this type of reverberation may distinguish 1-D anisotropic models from the two explanations typically offered for *SH*-motion in the teleseismic *P* wave-train: a) scattering due to velocity heterogeneities (e.g., VISSER and PAULLSEN, 1993; HU, 1993) and b) inclined interfaces beneath the receiver (e.g., OWENS and CROSSON, 1988; ZHU *et al.*, 1995). At any seismic station, more than one of these mechanisms may be important. If the azimuthal pattern of converted phases can be related confidently to a particular type of crustal model, stacking seismic records from different back-azimuths may be useful.

In this paper we investigate the influence of 1-D anisotropy, its type, layering and orientation, on the coda of teleseismic *P* waves, particularly on *P-SH* converted waves. We employ a reflectivity technique to compute the transmission response of a flat-layered medium with arbitrarily oriented hexagonally symmetric anisotropy, as developed by PARK (1996) for surface waves and extended by LEVIN and PARK (1977b) to receiver-function geometry. We describe the main features of synthetic seismograms for a variety of simple models and discuss how to interpret converted phases in observations.

Method

The models we consider consist of homogeneous flat layers atop a homogeneous halfspace. The halfspace is isotropic. Each layer may possess seismic an-

isotropy with an axis of symmetry $\hat{\mathbf{w}}$. The velocity profiles have Poisson ratio ≈ 0.27, consistent with a somewhat mafic continental crust (CHRISTENSEN, 1996). According to the classification by ZANDT and AMMON (1995), velocity values selected for the crust in our models would place them on the old stable continent. A compressional wave is assumed to propagate upwards from the halfspace into the layered part of the model, where it undergoes refraction and conversion. The combination of pulses arriving at the free surface is the "transmission response" of the media. Once computed, this transmission response can be convolved with the pulse of the original compressional wave, yielding a synthetic seismogram.

To compute the interaction of upgoing and downgoing plane waves, we express the elastic properties as a function of depth as $\mathbf{\Lambda}(z)$, where $\mathbf{\Lambda}_{ijkl}$ is the fourth-order stress-strain tensor. In the case where the axis of symmetry is horizontal, BACKUS (1965) derived the azimuthal dependence of P and SV velocities for horizontal propagation, which is appropriate for head waves in marine refraction studies. Expressed in terms of the angle ξ from $\hat{\mathbf{w}}$, these head-wave velocities are

$$\rho \alpha^2(\xi) = A + B \cos 2\xi + C \cos 4\xi$$

$$\rho \beta_{SV}^2(\xi) = D + E \cos 2\xi. \tag{1}$$

The SH velocity for horizontal propagation satisfies $\rho \beta_{SH}^2(\xi) = D + C(1 - \cos 4\xi) + E$.

If density perturbations are neglected, knowledge of A, B, C, D, E is sufficient to determine the stress-strain tensor (SHEARER and ORCUTT, 1986) for "weak" anisotropy. An expression for this tensor, outlined in the appendix, can be used for "strong" anisotropy as well. In an isotropic medium, $B = C = E = 0$ and $A = \lambda + 2\mu$ and $D = \mu$, where λ, μ are the Lamé parameters. PARK (1993) showed how these azimuthal relations generalize to other orientations of $\hat{\mathbf{w}}$. We assume a flat earth, $z = 0$ at the free surface, and z increasing downward.

To compute the reverberation response of a crustal model, we prescribe an upgoing plane-wave of the form $\mathbf{U}(\mathbf{x}, t) = \mathbf{u}_0 \, e^{i(\mathbf{k} \cdot \mathbf{x} - \omega t)}$ in the halfspace. A compressional plane wave in an anisotropic 1-D flat-layered structure suffers conversion to both vertically (SV) and horizontally (SH) polarized shear waves, with two exceptions: no P-SH conversion occurs if the axis of symmetry is everywhere vertical, or if the ray and the symmetry axis are contained in the same vertical plane in each layer.

The phase velocity for P and S waves in hexagonally symmetric media can be represented by smooth surfaces symmetric about the axis in 3-D-space defined by $\hat{\mathbf{w}}$ (Fig. 1). If $B, E > 0$, $\hat{\mathbf{w}}$ defines the 'fast' axis for wave propagation, leading to phase-velocity surfaces that resemble tilted melons. If $B, E < 0$, $\hat{\mathbf{w}}$ defines the 'slow' axis for wave propagation, leading to phase-velocity surfaces that resemble tilted pumpkins. The $\cos 4\xi$ coefficient C would distort these ellipsoidal surfaces. As noted in the appendix, departures from phase-velocity ellipticity can be substantial

in measurements made from sedimentary rock samples and for special cases in fine-layering anisotropy. However, the parameter C is small in most seismic refraction estimates (e.g., SHEARER and ORCUTT, 1986; ANDERSON, 1989). We also note in the appendix that the formulas of HUDSON (1981), CRAMPIN (1984) for crack-induced anisotropy imply either $C = 0$ or $C \ll B$. Although real-world anisotropy can be more complex than such observations and theories suggest, we set $C = 0$ in order to examine the large model space respresented by media with elliptical velocity surfaces of varying orientation, parameterized by $\hat{w}$, B, and E. Anisotropy of this simplified type has proven useful in modelling the azimuthal variation in both shear-wave splitting (BABUSKA *et al.*, 1993) and *P-SH* conversion LEVIN and PARK (1997a), so a careful examination of the relative influences of symmetry axis $\hat{w}$, S and P anisotropy is useful for the assessment of seismic data sets.

In a layer with constant anisotropic elastic properties, one can calculate three upgoing and three downgoing plane-wave solutions to the equations of motion, with vertical wavenumbers and polarizations determined by the eigenvectors of a

Anisotropy Parameterization
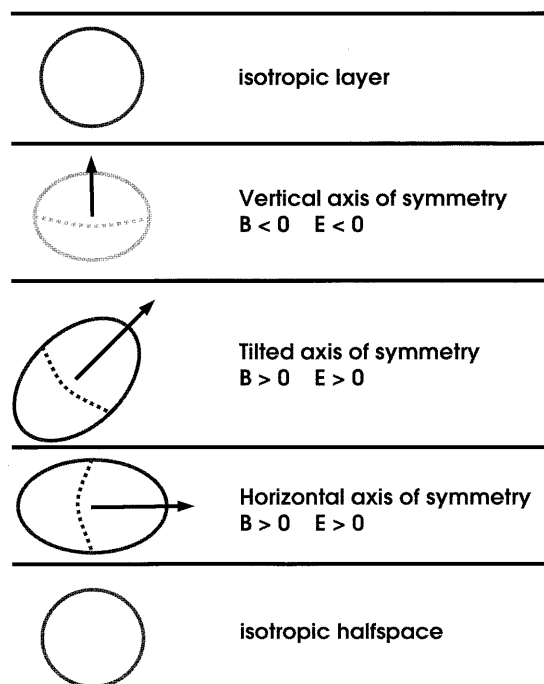
Figure 1
Schematic diagram illustrating possible shapes of velocity distribution for various choices of anisotropic parameters.
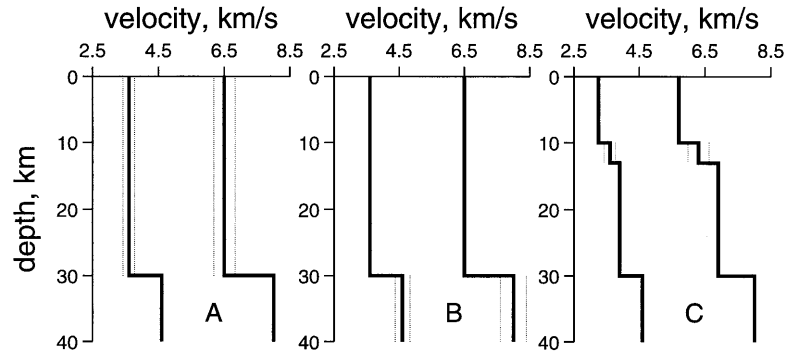
Figure 2

Schematic representation of 1-D velocity models used in simulations: a) anisotropic layer over an isotropic halfspace; b) isotropic layer over an anisotropic halfspace; c) thin anisotropic layer in an isotropic stack. Dashed lines denote range of velocity variation for 5% anisotropy (B, $E = -0.05$).

6×6 matrix eigenvalue problem (GARMANY, 1983; FRYER and FRAZER, 1987; PARK, 1996). Assume K layers over an isotropic halfspace, with interfaces at $z_1, z_2, \ldots z_K$. We compute the generalized transmission response of the layer stack, equivalent to a 3-D receiver function (LANGSTON, 1977), to determine the particle motion at the free surface $z_0 = 0$. A standard propagator formalism determines the response of a stack of anisotropic layers to upgoing wave motion with frequency ω and horizontal phase velocity c (slowness $p = 1/c$). We restrict attention to phase velocities c for which both P and S waves in the halfspace are oscillatory, thus bypassing the problem of leaky-mode reverberation. The algorithm follows the development of KENNETT (1983) closely, and is outlined in more detail in LEVIN and PARK (1997b) and PARK (1996). The transmission response of the medium is calculated at the evenly-spaced frequency values of the fast Fourier Transform of a chosen input wavelet. Particle motion at the surface is obtained by an inverse Fourier Transform. Noncausal 'wraparound' effects in this procedure are minimized by padding the initial wavelet with zeros in the time domain, to interpolate the spectrum.

Models, Ray Geometries and Procedures

We consider three distinct families of velocity models (Fig. 2): (A) an anisotropic layer over an isotropic halfspace; (B) an isotropic layer over a "thick" anisotropic layer; and (C) a "thin" anisotropic layer imbedded in an isotropic stack. In family A, the surface layer is anisotropic. In families B and C, the anisotropic layer is buried. For each model family we consider cases with P anisotropy only (coefficient B in (1)), S anisotropy only (coefficient E in (1)), and equal amounts of

P and *S* anisotropy. While anisotropy in *P* or *S* velocity only is hardly representative of physical reality, simulations with such an assumption provide insight into the relative contributions within "mixed" *P* and *S* anisotropy. The velocity models in family B place anisotropy in a layer below the Moho in the upper mantle, but the general behavior of these synthetic seismograms should carry over to the case of an anisotropic crustal layer overlain by a shallow low-velocity isotropic layer, e.g., a granite pluton atop anisotropic basement gneisses.

All waveforms analyzed in this work arise (through conversion and/or reverbertion) from the original compressional plane wave that ascends from the isotropic halfspace beneath the layers. Its pulse shape is prescribed at the bottom of the model, with all converted phases being scaled and/or distorted versions of it. No knowledge of the source of the pulse, or of the propagation effects in the medium outside our model is required for this exercise. In practice, effects of the source and the path outside the receiver region are routinely removed via "source normalization" techniques typical of receiver function analysis (e.g., LANGSTON, 1977).

Most synthetics are computed for 5% peak-to-peak velocity anisotropy (e.g., $B = 0.05$), with systematic variation in the tilt of the symmetry axis $\hat{w}$ and the back-azimuth of the arriving *P* wave. The effects of anisotropy magnitude and velocity contrast across the interface are studied in separate experiments. Both positive (fast symmetry axis—"melon") and negative (slow symmetry axis—"pumpkin") anisotropy are investigated, bringing the number of models examined within each family to 6. In all models the symmetry axis $\hat{w}$ is tilted at an angle η from the vertical towards the north, in 15° increments between 15° and 90°. (At $\eta = 0°$ the axis of symmetry is vertical and the *P-SV* and *SH* equations of motion are uncoupled.) We propagated upgoing plane waves through each of the anisotropic velocity models using a range of back-azimuths, measured clockwise from the north, and incidence angles. Incidence angles vary form 5° to 60° in 5° increments, and back-azimuths vary from 0° to 360° in 15° increments. Computations for 1800 plane waves were performed for each combination of the model family (A, B or C), anisotropy type (*P*, *S* or both) and the anisotropy sign (*B*, $E > 0$ or *B*, $E < 0$). In each simulation, the time-domain waveforms were computed and parameters (timing, amplitude, polarity) of the chosen phases were measured by a guided auto-picking routine.

An identical one-sided pulse waveform was used for the incoming *P* wave in all simulations. Sample synthetic seismograms for models from different families are shown on Figure 3. The converted phases most often have pulse shapes on the horizontal components that resemble either (1) a scaled version of the original pulse (e.g., the direct *P* in model-family A, and most radial phases) or (2) a derivative of the original pulse (e.g., the *Psms* phase in model-family A). In the first case the polarity of a converted phase is defined as "positive" if the pulse is "up," and the amplitude is defined as the maximum absolute value in a chosen time window. In the second case the phase polarity is considered "positive" if the first swing of the

pulse is "up." The amplitude of a waveform is then defined as a "peak-to-peak" difference between the smallest and the largest values within a chosen time window. These amplitude and polarity definitions, while not unique, are very helpful for describing how P-SH converted phases vary with the back-azimuth of the incident wave. Care was taken to design test models that would prevent an overlap of two phases in time. In real data overlapping phases may be unavoidable, and should be anticipated.

In the following sections we describe general properties of P-SH conversion in layered anisotropic media, present results of simulations for each model family and summarize common features. For each synthetic sweep the amplitudes of horizontal components are normalized by the maximum amplitude of corresponding vertical
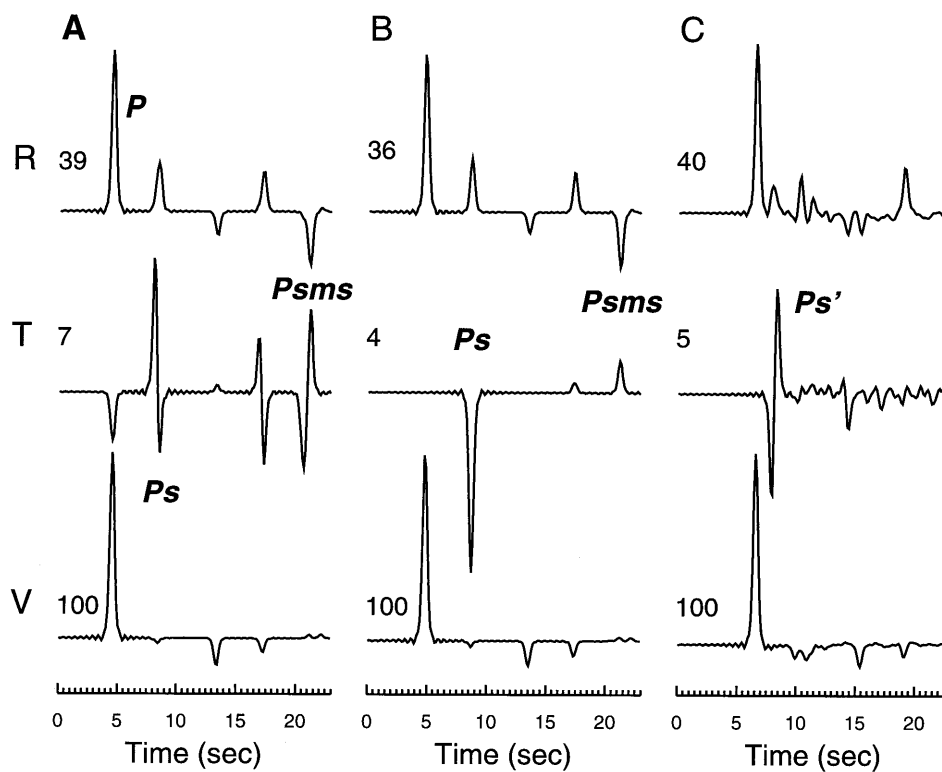
Figure 3

Sample waveforms generated in three velocity structures: a) anisotropic layer over an isotropic halfspace; b) isotropic layer over an anisotropic halfspace; c) thin anisotropic layer in an isotropic stack. Traces are scaled individually, with relative scale within each 3-component seismogram indicated by a number in percent at the beginning of each trace. Parameters of anisotropy used in simulations are: "melon" (positive) anisotropy of 5% in both P and S velocity, ray incidence angle 25%, back-azimuth 300°, axis tilt 60° from vertical. Converted phases analyzed in this paper are indicated for each model family.
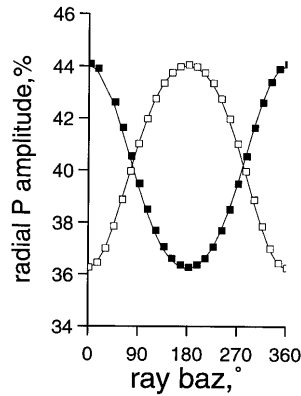
Figure 4

Azimuthal variation in the radial component of the direct *P* wave, model family A, pure *P* anisotropy. Incidence angle 30°, axis tilt 45° from vertical (maximal effect). Positive (melon) anisotropy imposes the pattern shown by open symbols, negative (pumpkin) anisotropy—solid symbols. Patterns are mirror-symmetric and vary as sin ξ with ray back-azimuth.

traces, and expressed in percent. For some converted phases, these amplitude ratios can vary with the period of the initial *P* pulse, especially if the phase is generated by two interfering pulses, as for the transverse component of shear-wave splitting. Therefore the amplitude ratios should be taken as guides to, rather than absolute predictions of, data behavior.

General Observations

The radial amplitudes of converted phases in anisotropic structures vary with incident back-azimuth, with unchanged polarity. The azimuthal pattern of the radial component is controlled by the tilt of the anisotropic symmetry axis, the incidence angle and the velocity contrast. The axis tilt angle η defines the shape of the pattern, whether two-lobed, four-lobed, or a composite. The incidence angle and the velocity contrast affect primarily the amplitude of the converted phase, and less so its azimuthal dependence. Figure 4 shows an amplitude pattern for one incidence angle and a sweep of back-azimuth that is representative of the phase behavior for the combination of model family and anisotropy type. The azimuthal patterns of radial-component converted phases are symmetric about the axis of symmetry $\hat{\mathbf{w}}$.

Variations of transverse components with incident back-azimuth are more complex, involving changes in both amplitude and polarity. Variations in incidence angle can lead to different azimuthal patterns independent of changes in other parameters. To describe fully the azimuthal pattern of the transverse-component of

the crustal phases, an area plot (Fig. 5) is required, similar in appearance to an earthquake focal mechanism. The azimuthal patterns of transverse-component converted phases are antisymmetric about the axis of symmetry $\hat{w}$. In addition to this polarity switch, azimuthal patterns of transverse phases often have a second set of polarity transitions, leading to a four-lobed pattern. The precise nature of these transitions depends on the anisotropic parameters and incidence angle. While it is usually marked by a moderate depression in amplitude values, pulse amplitude does not typically vanish at the secondary transition. Rather, a polarity transition occurs through a gradual evolution of the pulse shape (Fig. 6). For back-azimuth aligned with $\hat{w}$ there is no P-SH conversion, and the transverse component vanishes.

Systematic changes with back-azimuth ξ of amplitude, polarity and timing of converted phases have some 2-lobed dependence on $\sin \xi$ or $\cos \xi$ in all but special cases. However, secondary polarity and amplitude changes lead typically to asymmetric patterns, depending on the model parameters. Nevertheless, it is usually helpful to describe the azimuthal pattern by the number of lobes (2 or 4) in the complete 360°. For instance, the pattern in Figure 4 is two-lobed, while that in Figure 5 is asymmetrically four-lobed. In the special case of a horizontal symmetry
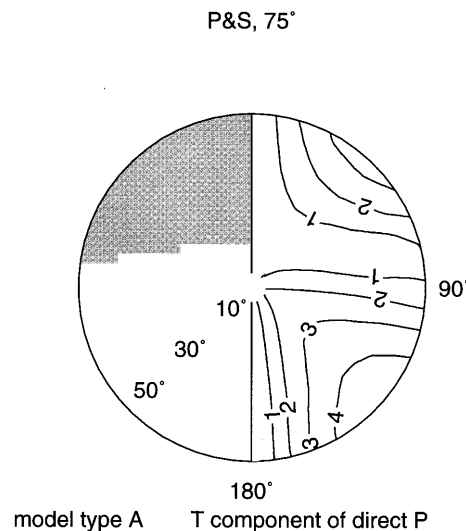
Figure 5
A diagram illustrating the azimuthal variation in amplitude and polarity of the transverse component of the direct P wave. Model family A, positive (melon) P and S anisotropy of 5%, axis tilt 75° from vertical. Right side of the plot illustrates variation of the amplitude (in percent of vertical P) as the function of back-azimuth and incidence angle. Back-azimuth varies clockwise from 0° to 180°. Incidence angle increases uniformly from 5° in the center to 60° at the rim. The left side of the plot illustrates polarity (shaded—negative) of the converted pulse for back-azimuths 180°–360°. Two sides of the plot are antisymmetric, since this is the transverse amplitude. In this example, pulses amplitudes for back-azimuths 180°–280° are positive, and for 80°–180° are negative.

model: P&S "melon", family A
axis tilt 60˚, incidence angle 30˚
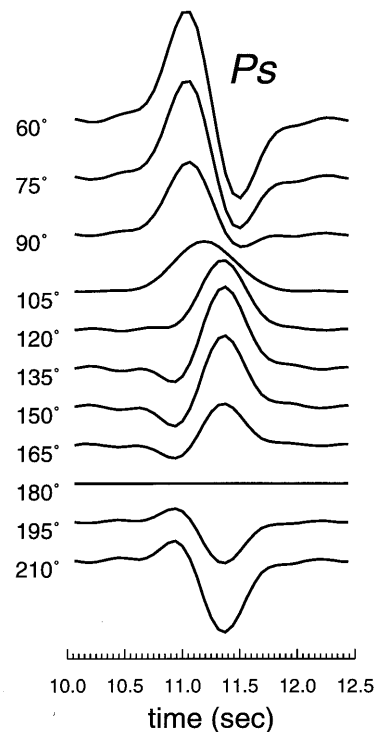
Figure 6

Pulse shape of a transverse *Ps* phase as a function of back-azimuth. Family A model with negative *P* and *S* anisotropy, $\eta = 60°$. Phane wave incidence angle 30°. Traces are plotted on a common scale, and labeled with ray back-azimuth. Change of polarity around BAZ 75° occurs via a gradual evolution of the waveform, while at 180° ($\hat{\mathbf{w}}$ direction) the transverse component vanishes.

axis $\hat{\mathbf{w}}$, all patterns are four-lobed and symmetric, and may by described by $\sin 2\xi$ or $\cos 2\xi$.

The transverse components of converted phases for opposite signs of anisotropy ("melon" vs. "pumpkin") always have opposite polarity, leading to mirror-image azimuthal patterns. In most cases the radial components of converted phases also display mirror symmetry in models with opposite anisotropy sign. Exceptions from this rule are discussed in following sections.

The effects of *P* and *S* anisotropy differ substantially. The effect of pure *P* anisotropy is typically two-lobed, and is maximized when the symmetry axis $\hat{\mathbf{w}}$ is tilted at $\eta = 45°$. The effect of pure *S* anisotropy is more four-lobed, and is strongest for subhorizontal $\hat{\mathbf{w}}$. If the anisotropy types are mixed, the azimuthal patterns follow the stronger influence.

Model Family A: Anisotropic Layer over an Isotropic Halfspace

Because the polarization of seismic waves is distorted within the surface layer by its anisotropy, each phase for this family of models typically has a transverse component. Polarization distortion also affects the radial component amplitude significantly. The radial component of the direct P wave suffers a two-lobed perturbation to its amplitude in the presence of P anisotropy (Fig. 7). The intensity of the pattern depends on the tilt of the symmetry axis. Radial P amplitudes are also affected by S anisotropy, which imposes a weak four-lobed perturbation. An equal combination of P and S anisotropy generates amplitude perturbations that resemble those of the pure P case. The transverse component of the P phase is not a P-SH converted phase, but rather a compressional motion deflected out of the source-receiver plane. The most pronounced effect is observed for pure P an-isotropy (Fig. 8). Depending on the tilt angle η, the amplitude patterns are either two- or asymmetrically four-lobed.

P-to-S conversion at the base of the anisotropic layer follows direct P on our synthetic seismograms. In the presence of S-wave anisotropy its timing on the radial component relative to the direct P follows a four-lobed azimuthal pattern (Fig. 9), as would be expected from the introduction of $\cos 2\xi$ variations in shear velocity. Peak-to-peak variation of almost half a second is reached in our models for near-horizontal orientation of anisotropy axis, as the shear wave (Ps) traverses the entire crust in the model. The presence of P anisotropy in the surface layer adds a smaller, but nonzero, perturbation to the P-Ps delay time.
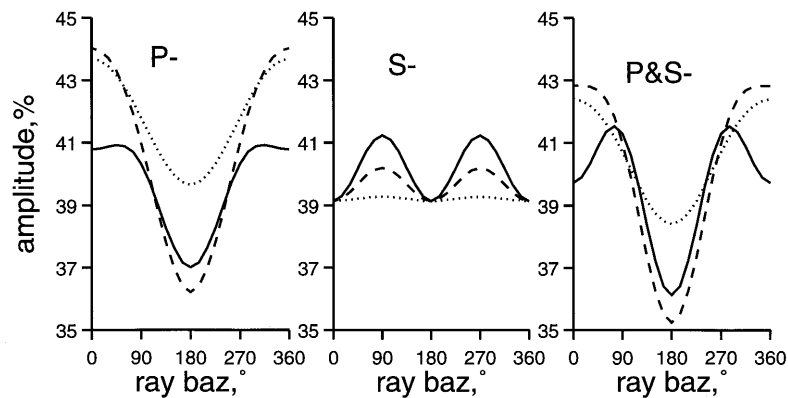
Figure 7

Radial component of the direct P wave as a function of back-azimuth in family A models with negative (pumpkin or "$-$") anisotropy. Incidence angle of the incoming wave is 25°. The line type indicates the tilt from vertical of the anisotropic symmetry axis: dotted $-15°$, dashed $-45°$, solid $-75°$. Type of anisotropy (P-, S- or combined) is indicated on the plots.
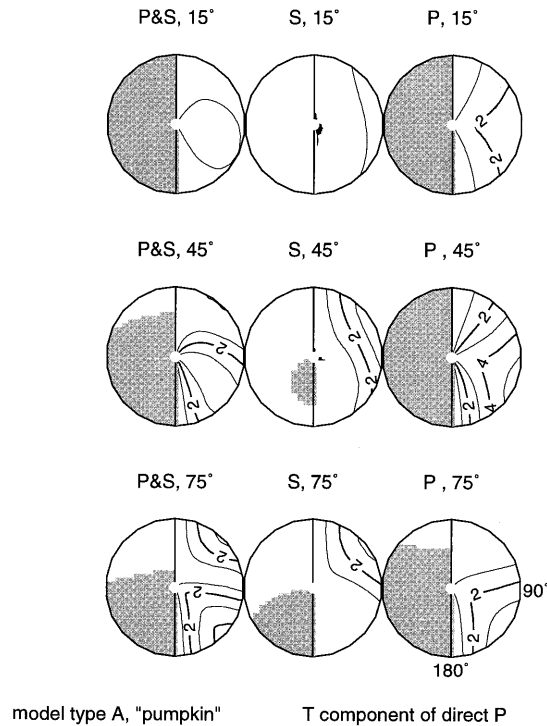
Figure 8

Transverse component of the direct *P* wave in family A models with negative anisotropy as a function of back-azimuth, incidence angle and anisotropic axis tilt from vertical. Parameters of radial plots are as in Figure 5. Anisotropy type and anisotropic axis tilt from vertical are indicated above each plot.

The radial amplitude of the *Ps* phase can change by more than a factor of 2 in the presence of *P* anisotropy (Fig. 10a). The azimuthal pattern is two-lobed. Pure *S* anisotropy causes much smaller variations in the radial *Ps* phase (Fig. 10b). In a deviation from typical behavior, a change from a "pumpkin" to a "melon" anisotropy (i.e., the sign of the anisotropic parameters *B* and *E*) affects the amplitude of the transverse *Ps* phase slightly without altering the distribution of lobes in the azimuthal pattern. This subtle change is not likely to be a useful interpretive tool for observations, however.

A combination of *P* and *S* anisotropy results in azimuthal patterns that depend strongly on the axis tilt (Fig. 10c). Axes inclined no more than 45° result in two-lobed amplitude patterns that are relatively smooth. *Ps* amplitude perturbations for opposite signs of anisotropic parameters *B* and *E* resemble mirror images of each other. If the axis of symmetry $\hat{\mathbf{w}}$ is subhorizontal, however, *Ps* amplitude oscillates rapidly with back-azimuth. This pattern is sufficiently asymmetric to cause, in the case of the "pumpkin" (negative) anisotropy, *Ps* amplitudes from
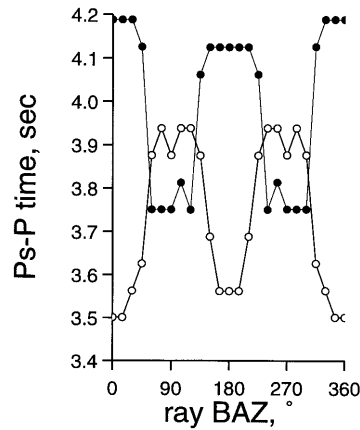
Figure 9

Timing of *Ps* phase in family A models with positive (open symbols) and negative (closed symbols) *P* and *S* anisotropy. Values are computed for the ray incidence angle 25°, and a symmetry axis tilted 75° from vertical. For this incidence angle, 75° tilt yields the largest azimuthal variation of *Ps-P* delay.

back-azimuths subparallel to $\hat{\mathbf{w}}$ that exceed those from other directions by almost a factor of 2 on the radial component.

The transverse component of *Ps* phase can be as large as 15% of *P* in our synthetic seismograms (Fig. 11). Near-vertical incidence leads to converted waves with small amplitudes ($\lesssim 5\%$), leaving the largest converted-wave amplitudes to shallow-incidence *P* waves. Azimuthal patterns obtained in models with pure *P* anisotropy are generally two-lobed, with two additional smaller lobes appearing in the pattern for
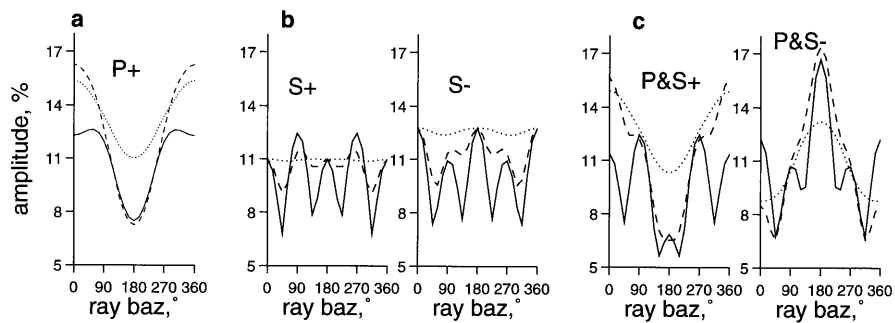
Figure 10

Radial component of the *Ps* phase in family A models. Type and sign of anisotropy is indicated on the plots. The line type indicates the tilt of the anisotropic symmetry axis from vertical: dotted $-15°$, dashed $-45°$, solid $-75°$, a) Pure *P* anisotropy. b) Pure *S* anisotropy. Distribution of lobes in the azimuthal pattern is not sensitive to the sign of anisotropy; c) *P* and *S* anisotropy. Azimuthal patterns strongly depend on η.
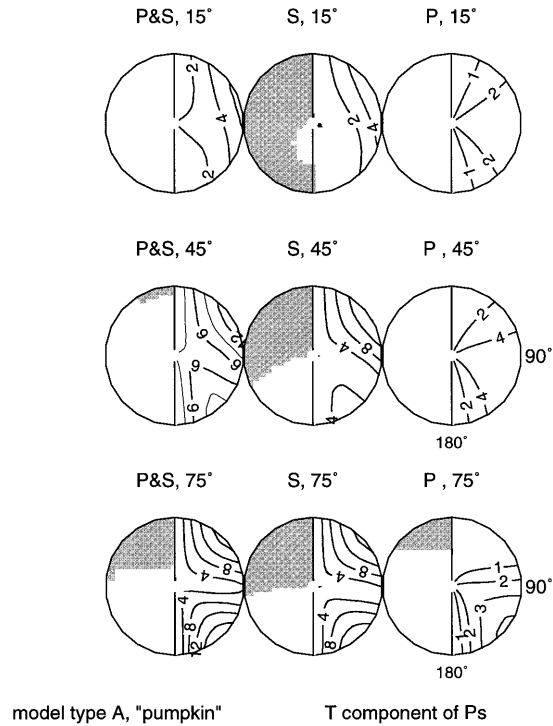
Figure 11

Transverse component of the *Ps* phase in family A models with negative anisotropy. Parameters of area plots are as in Figure 5. Anisotropy type and anisotropic axis tilt from vertical are indicated above each plot.

near-horizontal axes and relatively shallow incidence. In models with *S* velocity anisotropy the azimuthal pattern of transverse *Ps* amplitudes is always four-lobed, with relative sizes of the lobe pairs controlled by the anisotropic axis tilt. Transverse-component amplitude in the case of *P* anisotropy is relatively small. For *S* anisotropy, derivative-pulse shapes on the transverse component indicate that much of this waveform arises from a shear-wave splitting time delay δt. The relative amplitude of the transverse component therefore depends on the ratio of δt to the period *T* of the incoming wave i.e., stronger for shorter period waves, weaker for longer-period waves.

The *Psms* phase arrives between 15 and 17 seconds after the direct *P* in our simulations. It is a split shear wave, generated through a substantial *P-S* conversion at the free surface and subsequently reflected back from the top of the halfspace. The *Psms* phase is very prominent on the transverse component if there is *S* wave anisotropy in the model (Fig. 12), as a result of shear-wave splitting. The delay time

of the *Psms* arrival, relative to *P*, is only slightly affected by the presence of anisotropy, because both fast and slow *S* polarization contribute to the waveform. For symmetry-axis tilts $\eta > 45°$, the amplitude of this phase can be as large as 15% that of direct *P*, forming four-lobed azimuthal patterns.

Model Family B: Isotropic Layer over Anisotropic Halfspace

In synthetic seismograms computed for this model family, *Ps* is the first arrival on the transverse component. Its delay relative to the direct *P* varies insignificantly with back-azimuth. The radial component of the direct *P* wave is also nearly constant as back-azimuth varies. The amplitude of the radial component of the *Ps* phase, on the other hand, can change by as much as a factor of 2 in a two-lobed azimuthal pattern (Fig. 13). The transverse component of *Ps* is larger (up to 5%) in
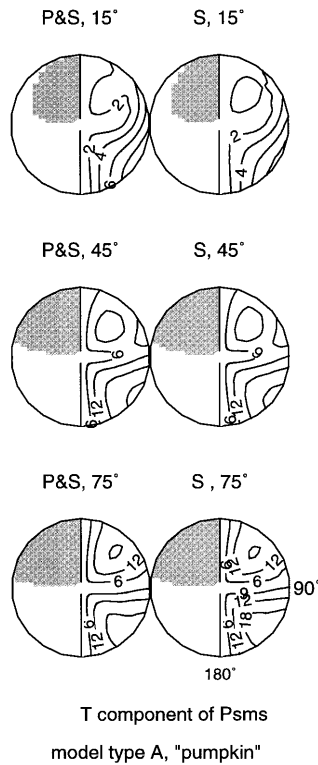
Figure 12

Transverse component of the *Psms* phase in family A models with negative anisotropy. Parameters of area plots are as in Figure 5. Anisotropy type and anisotropic axis tilt from vertical are indicated above each plot.
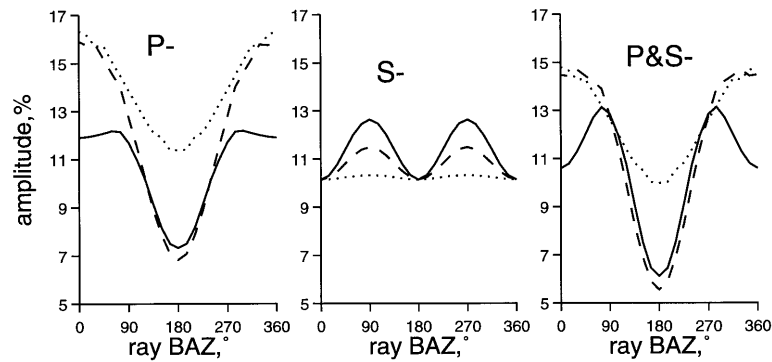
Figure 13

Radial component of the *Ps* phase in family B models. The line type indicates the tilt of the anisotropic symmetry axis from vertical: dotted −15°, dashed −45°, solid −75°. Type of anisotropy is indicated on the plots.

models with *P* anisotropy than in models with pure *S* anisotropy (Fig. 14). Azimuthal patterns of transverse *Ps* amplitude change from two-lobed for subvertical axes to asymmetric four-lobed for subhorizontal axes. The transverse amplitude of the *Psms* phase does not exceed 3% in any of our simulations, with *S* anisotropy models leading to stronger conversions, largely due to the lack of shear-wave splitting in the isotropic surface layer. Azimuthal patterns are mostly two-lobed, with two vestigial lobes present if the symmetry axis $\hat{\mathbf{w}}$ is subhorizontal.

Model Type C: Thin Anisotropic Layer in an Isotropic Stack

Many parameters influence the *P* coda generated in this family of models. The ratio of wave period *T* to the travel time through the anisotropic layer is one of the strongest influences, as it determines whether the converted phases generated at the upper and lower boundaries of the anisotropic zone interfere or arrive as separate pulses. We used a velocity-depth profile in which the sense of velocity contrast across all boundaries does not change if 5% anisotropy is introduced into a thin intermediate layer (Fig. 2c). This type of model would be appropriate, for instance, for a shear zone within the crust (COLEMAN, 1996). Other scenarios may be necessitated by particular datasets (e.g., a direction-dependent low-velocity zone), but we defer their investigation.

The radial component of the direct *P* wave does not vary significantly with back-azimuth. The first-arriving energy on the transverse component is the equivalent of the *Ps* phase (labeled *Ps'* to distinguish it from *P*-to-*S* conversion at the base of the "crust"). This phase, composed of two pulses of opposite polarity generated

at the two interfaces bounding the anisotropic layer, dominates the transverse component in the presence of *P* anisotropy. The separation between the two pulses depends on the layer thickness and the dominant period of the incident waveform. Because interference between converted phases is what distinguishes model family C from earlier cases, we scaled the thickness of the intermediate layer to examine these effects (Fig. 3c). The timing of the *Ps′* phase relative to the direct *P* arrival is determined by the depth of the imbedded layer and is only weakly affected by the presence of anisotropy in it.

The azimuthal variation of the radial component of the *Ps′* phase is shown on Figure 15. Significant changes in amplitude with azimuth are seen only for the models containing *P* velocity anisotropy. The azimuthal patterns are four-lobed, with the relative size of lobes strongly dependent on the axis tilt. The amplitudes of the transverse component of *Ps′* reach 10% in our simulations, with *P* wave anisotropy leading to considerably stronger converted phases. The azimuthal patterns (Fig. 16) change from two-lobed for subvertical $\hat{w}$ to asymmetric four-
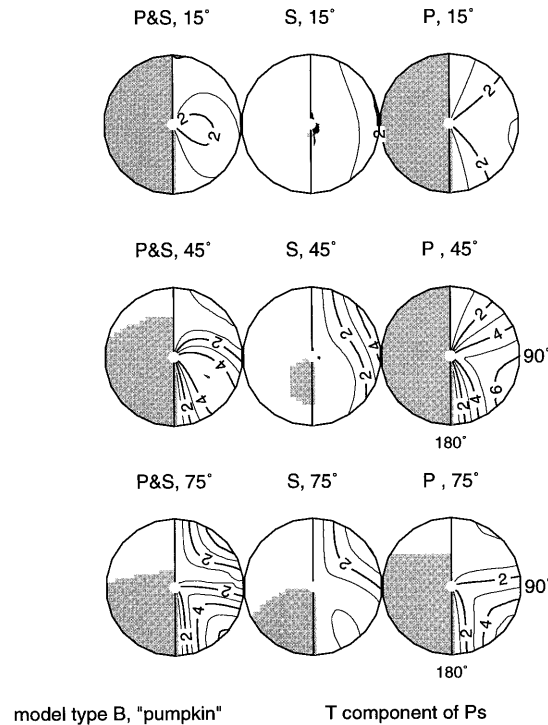
Figure 14
Transverse component of the *Ps* phase in family B models with negative anisotropy. Parameters of area plots are as in Figure 5. Anisotropy type and anisotropic axis tilt from vertical are indicated above each plot.
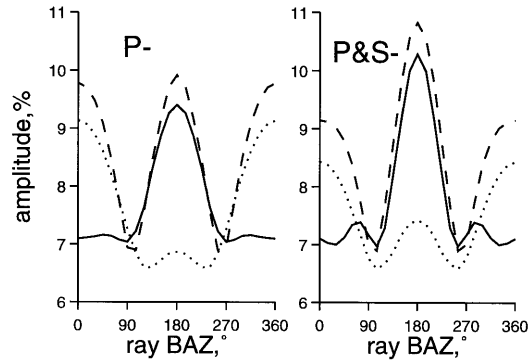
Figure 15

Radial component of the *Ps'* phase in family C models with negative anisotropy. Significant variation of radial amplitude is seen only if *P* anisotropy is present in the model. The line type indicates the tilt of the anisotropic symmetry axis from vertical: dotted −15°, dashed −45° solid −75°. Type of anisotropy is indicated on the plots.

lobed for subhorizontal $\hat{w}$. The raypath through the anisotropic layer is too short to induce substantial shear-wave splitting, so this patterns depends more on the details of wave conversion at the interfaces. In another deviation from the general tendency, only the radial amplitudes of *Ps'* are affected by a change of sign in the anisotropic parameters *B* and *E*, while the lobe patterns are similar for both "melon" and "pumpkin" models.

Reverberations in a model containing three layers over a halfspace lead to synthetic seismograms sufficiently complex to make later arrivals more difficult to associate with particular interfaces. Although numerous phases comparable in amplitude with *Ps'* appear in synthetics computed for pure *S* anisotropy, their origin and properties are likely to be very model-specific. By extension, multiple-layer models with distinct anisotropic parameters in successive layers will often lead to *P* coda that are difficult to interpret.

Special Case—Horizontal Symmetry Axis

Most studies of shear-wave splitting due to seismic anisotropy assume that the axis of symmetry $\hat{w}$ is horizontal. This assumption is also made by KOSAREV *et al.* (1984), FARRA *et al.* (1991) and VINNIK and MONTAGNER (1996) to analyze *P-SH* conversions from upper-mantle discontinuities. In our synthetics, the azimuthal patterns of converted phases that develop for horizontal axes of anisotropy are qualitatively similar to the "near-horizontal" cases in each model family. The main distinguishing feature of *SH* waveforms in the horizontal axis models is an exact

$\sin 2\xi$ symmetry in the amplitude patterns. Zero amplitude nodes occur both parallel and at 90° to the symmetry-axis direction, and all four lobes of the pattern are of the same size.

Other Parameters, Other Effects

The velocity contrast across an interface in an anisotropic medium controls the process of *P-SH* conversion, as it controls *P-SV* conversion in the isotropic case: the amplitude of *SH*-type motion scales directly with the velocity jump across the interface (Fig. 17). Converted-phase amplitudes are enhanced with an increase in the incidence angle. An exception is the transverse component of the direct *P*, which depends primarily on polarization distortion in the surface layer, and only weakly on the velocity contrast of the interface.
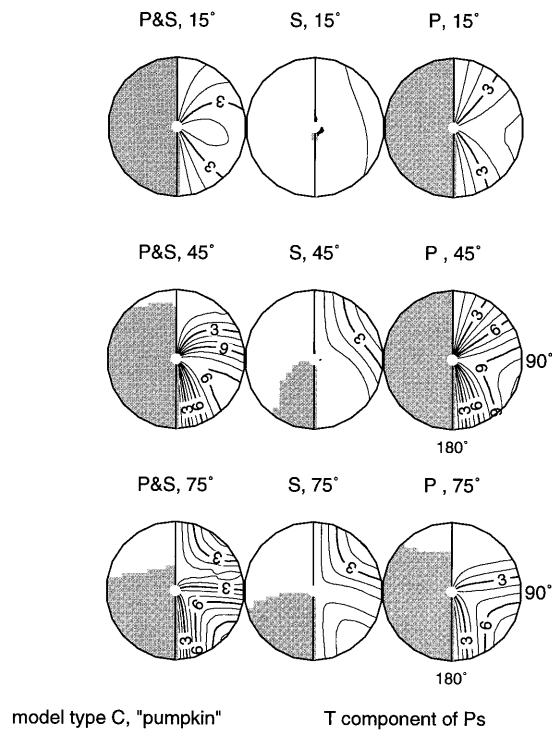
Figure 16
Transverse component of the *Ps'* phase in family C models with negative anisotropy. Parameters of area plots are as in Figure 5. Anisotropy type and anisotropic axis tilt from vertical are indicated above each plot.
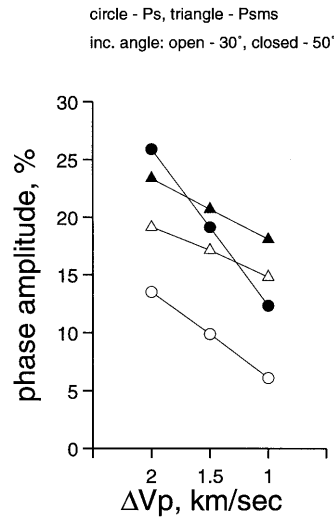
Figure 17
Influence of the velocity contrast across an interface on the *P-SH* conversion. Compressional velocity values of 6.0, 6.5 and 7.0 km/sec were used for the anisotropic layer over an isotropic halfspace with compressional velocity 8.0 km/sec (model family A). Shear velocity values were computed as $Vp/1.8$. A positive (melon) anisotropy of 5% in both *P* and *S* velocities were used in the layer. The plot depicts amplitudes of transverse *Ps* (circles) and *Psms* (triangles) phases for rays incoming from back-azimuth 315° with an incidence angle of 30° (open symbols) and 50° (closed symbols).

The magnitude of anisotropy (i.e., the value of *B* and/or *E* coefficients in (1)) directly scales the amplitude of resulting *P-SH* conversions. Stronger anisotropy leads to azimuthal patterns that are more differentiated but have nodes (polarity changes) in the same places. It should be noted that direct dependence of converted-phase parameters on velocity contrast and anisotropy extent holds only as long as the sense of velocity change across the interface is preserved. These relationships will break down if the velocity difference across the interface is comparable to the anisotropic perturbation. In an extreme case, a directionally-dependent velocity inversion may exist, so that different phases may be generated for different combinations of incidence angle, axis orientation and ray back-azimuth.

Discussion

The effects of anisotropy one may hope to interpret successfully in *P* coda involve both the presence of transverse motions (the phases *Ps* and *Psms* and the transverse component of direct *P*), as well as the azimuthal variation of radial amplitudes (*P* and *Ps*). Synthetic seismograms for a variety of simple 1-D an-isotropic velocity models allow us to make a number of observations, and to

propose answers for the questions posed at the onset of this study. The major lesson drawn from this exercise is the importance of P anisotropy in the generation of P-coda from teleseismic body waves, as well as the strong sensitivity of P-to-S converted phases to the tilt of the symmetry axis of anisotropy. Most anisotropy studies, aside from large-scale tomographic experiments, assume a horizontal or vertical axis of symmetry and interpret data in terms of S anisotropy only. Our experiments suggest that this may be too restrictive.

Models with a surface anisotropic layer (family A) are most efficient in generating P-SH conversions in our experiments. Ps and $Psms$ with amplitudes on the order of 10% of the vertical P will be observed for incidence angles over 20°. A transverse component of the direct P is a diagnostic phase of this model type, indicating that anisotropy extends all the way up to the receiver. Also diagnostic is the azimuthal dependence of the P-Ps phase timing, and strong azimuthal variation in the radial component of the direct P.

A delayed first motion on the transverse component is diagnostic of models in families B and C, in which the anisotropic layer is buried. For simple models with a single anisotropic layer, the P-SH converted phase would likely be the most energetic transverse arrival as well. The timing of this arrival relative to direct P may be the best indicator of the depth of the buried anisotropic layer. Since the surface layer is isotropic in both model families B and C, the variation of Ps-P delay times is negligible, as is the variation in radial amplitude of direct P. A possible discriminant between types B and C is the azimuthal variation of the radial Ps phase. If the symmetry axis $\hat{\mathbf{w}}$ is tilted 45°, the pattern is two-lobed if the layer is buried and "thick" (family B) and four-lobed if the anisotropic layer is buried and "thin" (family C). It is instructive that both B and C model families yield significant P-SH conversions only if P-wave anisotropy is present. Speculatively, a thin layer of anisotropy within the crust may prove to be more appealing in crustal models than the "anisotropic halfspace" concept. It is also instructive that large transverse-component P coda can be generated with anisotropic layers that are too thin to generate significant shear-wave splitting. The derivative-pulse shape characteristic of the Ps' phase in model family C (Fig. 3) resembles a split shear wave, but actually is generated by the interference of P-to-S conversions at separate interfaces. To distinguish between this type of effect and that of an anisotropic layer above the P-to-S conversion, one might check for a transverse component in direct P due to polarization distortion, and the transverse component of a "$Psms$" phase, generated by P-to-S conversion at the free surface.

It seems that discriminating the "melon" and the "pumpkin" models of anisotropy on the basis of P-SH converted data may be difficult with P coda observations only, as the azimuthal patterns of most phases are similar. In model family A the pattern of the radial Ps phase may help determine the sign of anisotropy. Also a comparison of Ps-P delay pattern with that of the direct P amplitude may be instructive. However, supplementary data may be necessary to

distinguish directly whether inferred anisotropy is due to cracks or thin layering ("pumpkin") or LPO of mineral fast-axes ("melon").

Stacking *P* coda to enhance converted phases is potentially a powerful tool. If the symmetry axis $\hat{w}$ throughout the crust and shallow mantle is horizontal, stacking with cos 2ξ- and sin 2ξ-weighting with back-azimuth ξ should enhance the signal-to-noise ratio and identify the strike of $\hat{w}$. Likewise, the effects of *P* and *S* anisotropy are quite similar for horizontal $\hat{w}$. Although this makes distinguishing *P* from *S* anisotropy difficult from seismic data alone, the tradeoff between the two is straightforward. However, if the axis is tilted, the converted-phase azimuthal patterns can be four-lobed, two-lobed or a mixture of the two. The two anisotropy types behave differently as $\hat{w}$ varies from horizontal to vertical, making data interpretation more challenging.

Conclusions

Seismic anisotropy in a flat-layered homogeneous medium results in the generation of *P-SH* converted phases and also affects *P-SV* conversions. Since the anisotropy of many rocks can be approximated to possess either a fast or slow axis of symmetry, we have used hexagonal symmetry in our calculations, varying the orientation of the symmetry axis $\hat{w}$. *P-SH* conversions arise in models containing either *P* and/or *S* velocity anisotropy, with *P* anisotropy leading to stronger effects in many of the scenarios we examined. Synthetic *P* coda from different combinations of anisotropy type, sign and location are substantially distinct, and potentially resolvable in band-limited noisy data.

The strengths of *P-SV* and *P-SH* conversions vary with the back azimuth ξ of the incoming wave relative to the axis of symmetry $\hat{w}$. These patterns can be used to distinguish candidate models of anisotropy. The tilt of the anisotropic symmetry axis and the incidence angle of the incoming *P* wave control the resulting azimuthal pattern. Perturbative waveforms on the radial component, whether due to converted phases or polarization distortions of direct *P*, are symmetric to sign changes in ξ. Perturbative waveforms on the transverse component are anti-symmetric to sign changes in ξ. Near-vertical axes of symmetry result in azimuthal patterns that are effectively two-lobed (sin ξ). A transition to asymmetric four-lobed pattern occurs with increasing tilt and is more pronounced for shallow incidence *P* waves. The perturbative waveforms often do not vanish at the pair of "nodes" that define extra lobes in the azimuthal pattern, but rather distort gradually in a manner that makes the precise location of the polarity transition somewhat subjective. Patterns with exact sin 2ξ and cos 2ξ symmetry, and waveforms that vanish at the second set of polarity transitions, occur only when the axis of symmetry $\hat{w}$ is horizontal. The effect of pure *P* anisotropy is maximized when the symmetry axis $\hat{w}$ is tilted 45° from the vertical, while the effect of pure *S* anisotropy is strongest for subhorizon-

tal axes. In the case of mixed anisotropy, azimuthal patterns follow the stronger influence. For subvertical axis tilts, models with pure P and pure S anisotropy predict transverse Ps patterns of opposite polarity. Aside from a few cases, changes of anisotropy sign, that is, switching between slow and fast axes of symmetry, results in azimuthal patterns that are mirror images of each other.

Our synthetic P coda suggest that interference between P-to-S converted phases from different interfaces within the crust can create SH-waveforms that resemble the derivative-pulse waveforms diagnostic of shear-wave splitting. Paradoxically, these phases are best generated by thin layers of compressional, not shear, anisotropy with a tilted axis of symmetry.

Acknowledgments

Appendix: Relation to THOMSEN (1986)

Anisotropy with *one* axis of symmetry can be parameterized by seven constants, two of which describe the orientation of the axis of symmetry $\hat{\mathbf{w}}$, and five elastic parameters. Several choices for the five elastic parameters exist in the literature (ANDERSON, 1989). The choice we take in (1) was initially derived for weak anisotropy with a horizontal axis of symmetry in the context of marine refraction studies (BACKUS, 1965). In the limit of weak anisotropy, the coefficients in (1) can be related directly to a decomposition of the elastic tensor, each term of which possesses hexagonal symmetry with respect to rotations about $\hat{\mathbf{w}}$ (SHEARER and ORCUTT, 1986). We express the elastic tensor in each layer with the following decomposition:

$$\mathbf{\Lambda} = A\mathbf{\Lambda}_A + B\mathbf{\Lambda}_B + C\mathbf{\Lambda}_C + D\mathbf{\Lambda}_D + E\mathbf{\Lambda}_E, \tag{2}$$

where

$$\mathbf{\Lambda}_A = \mathbf{I} \otimes \mathbf{I}$$
$$\mathbf{\Lambda}_B = \mathbf{W} \otimes \mathbf{I} + \mathbf{I} \otimes \mathbf{W}$$
$$\mathbf{\Lambda}_C = 8\mathbf{W} \otimes \mathbf{W} - \mathbf{I} \otimes \mathbf{I} \tag{3}$$

$$\Lambda_D = {}_{(13)}\mathbf{I} \otimes \mathbf{I} + {}_{(14)}\mathbf{I} \otimes \mathbf{I} - 2\mathbf{I} \otimes \mathbf{I}$$

$$\Lambda_E = 2[{}_{(13)}\Lambda_B + {}_{(14)}\Lambda_B - 2\Lambda_B] + \Lambda_D.$$

The '$\otimes$' symbol denotes the tensor product operation, and $\mathbf{W} = \hat{\mathbf{w}} \otimes \hat{\mathbf{w}} - \frac{1}{2}\mathbf{I}$, where $\mathbf{I}$ is the identity tensor. The permutation (ij) indicates the interchange of the ith and jth tensor index e.g., $\{{}_{(13)}\mathbf{I} \otimes \mathbf{I}\}_{ijkl} = \delta_{kj}\delta_{il}$. An isotropic elastic tensor $\Lambda^{(0)}$ contains only terms proportional to the isotropic tensors Λ_A and Λ_D, as neither depends on $\hat{\mathbf{w}}$.

When using expressions (2) and (3), we are neither limited to "weak" anisotropy nor to a horizontal axis of symmetry. For "strong" anisotropy, PARK (1996) shows that the azimuthal phase velocity formulas (1) are the first-order approximations to the P and SV head-wave velocities of a medium with horizontal $\hat{\mathbf{w}}$ and elastic tensor described by (2) and (3). For modeling media with more complexity, it is possible to form a linear combination of anisotropic deviations from an isotropic reference model, each with its own axis of symmetry $\hat{\mathbf{w}}$. This would be useful for media with both oriented cracks and oriented minerals, if the orientations differ, or for media with orthorhombic symmetry.

Another common parameterization for hexagonally-symmetric anisotropy is that derived by THOMSEN (1986) for a vertical axis of symmetry in the context of shallow seismic profiling. Thomsen references phase velocities to the vertical velocity, rather than to the average of the velocity extremes, with three anisotropic parameters γ, ε and δ^*. In applications, Thomsen recommends replacing δ^* with a first-order approximation "δ". To relate these parameters to our anisotropic parameters B, C, and E, we can use the formulas of YU and PARK (1993) to express the elastic tensor 6×6 matrix format $\{C_{jk}\}$ for a vertical axis of symmetry. We adopt the usual conventions, with components 1, 2, 3 corresponding to x, y, z, respectively, and $C_{jk} = \Lambda_{lmnp}$ according to the substitutions $1 \rightarrow 11$; $2 \rightarrow 22$; $3 \rightarrow 33$; $4 \rightarrow 23$; $5 \rightarrow 13$; and $6 \rightarrow 12$. The matrix $\mathbf{C}$ is expressed as

$$
\begin{bmatrix}
A-B+C & A-B+C-2(D-E) & A-3C-2(D+E) & & & \\
A-B+C-2(D-E) & A-B+C & A-3C-2(D+E) & & & \\
A-3C-2(D+E) & A-3C-2(D+E) & A+B+C & & & \\
& & & D+E & & \\
& & & & D+E & \\
& & & & & D-E
\end{bmatrix}
$$

$$(4)$$

where the blank indices are zero. Using the formulas in PARK (1996), the Christoffel matrix $\mathcal{K}$ for this elastic tensor can be computed for an upgoing plane wave at an angle of incidence θ to the vertical, using wavenumber vector $\mathbf{k} = \hat{\mathbf{x}} \sin \theta - \hat{\mathbf{z}} \cos \theta$. (Note that z increases downward in the coordinate system of our synthetic-seismogram calculations.)

$$\mathcal{K} = \begin{bmatrix} (A-B+C)\sin^2\theta + (D+E)\cos^2\theta & 0 & -(A-3C-D-E)\sin\theta\cos\theta \\ 0 & D+E\cos 2\theta & 0 \\ -(A-3C-D-E)\sin\theta\cos\theta & 0 & (A+B+C)\cos^2\theta + (D+E)\sin^2\theta \end{bmatrix}$$

(5)

The eigenvalues of the Christoffel matrix correspond to the phase velocities of the quasi-*P*, quasi-*SV* and quasi-*SH* polarized waves. These phase velocities correspond to those derived by THOMSEN (1986).

Using (4), we can relate the two sets of anisotropic parameters, using Thomsen's definitions

$$\varepsilon = \frac{C_{11} - C_{33}}{2C_{33}} = -\frac{B}{A+B+C}$$

$$\gamma = \frac{C_{66} - C_{44}}{2C_{44}} = -\frac{E}{D+E}$$

$$\delta = \frac{(C_{13} + C_{44})^2 - (C_{33} - C_{44})^2}{2C_{33}(C_{33} - C_{44})} = \frac{8C^2 - B^2 - 2BC - 2(B+4C)(A-D-E)}{2(A+B+C)(A+B+C-D-E)}.$$

(6)

The first two of Thomsen's parameters relate directly to our parameters *B* and *E* for the $\cos 2\xi$ azimuthal variation in phase velocity. The negative sign in the formulas for ε and γ reflects the preponderance of "slow" symmetry axes in crustal environments, corresponding to crack and/or fine-layering anisotropy. The formula for δ is complex, but can be reduced by discarding higher-order terms to obtain

$$\delta \approx \varepsilon - \frac{4C}{A+B+C}$$

(7)

From this formula, one infers that the phase velocity surface for quasi-*P* waves is elliptical only if $\varepsilon = \delta$. This condition is not satisfied for many of the anisotropy measurements tabulated in THOMSEN (1996), indicated that $C = 0$ might be an incorrect assumption. However, extending these measurements to characterize crystalline bedrock may be risky. All elastic properties tabulated in THOMSEN (1986) involve shallow sedimentary facies relevant to oil exploration, with relatively few values measured *in situ*. For the *in situ* measurements of seismic anisotropy tabulated in THOMSEN (1986), $\varepsilon \approx \delta$ tends to be better satisfied. This suggests an enhancement of *C* by decompression, perhaps via an increase in the porosity of a rock sample.

The case for setting $C = 0$ in our calculations is supported by the perturbative expressions for anisotropy in cracked isotropic media (HUDSON, 1981; CRAMPIN, 1984). These expressions estimate that $B = C = 0$ for fluid-saturated cracks, and, using (4), one can show that $C = 0$ of the first-order perturbation associated with dry cracks. In the second-order dry-crack perturbation in a Poisson solid, $C/B \lesssim 0.1$, suggesting that *P*-phase velocities are near-elliptical for this case, in Hudson's perturbation theory at least.

A suggestion that C might typically be nonzero arises from a special case in the theory for anisotropy caused by thin-layering of different media (BACKUS, 1962; HELBIG, 1994; THOMSEN, 1986). In this theory, Thomsen's parameter $\delta \approx 0$ if the alternating lithologies share a common Poisson ratio. This is equivalent to $C = -B/4$, a small value, but not zero. However, constant Poisson ratio is not the norm among crustal rocks. A typical intercalation in the crystalline basement might involve felsic and mafic rock types, where the mafic layers have higher seismic velocities α, β *and* higher Poisson ratio (i.e., a higher velocity ratio α/β). Using the averaging formulas in Chapter 7.4 of HELBIG (1994), one can demonstrate that $B < 0$ and $0 \leq (B + 4C)/B \leq 1$ for this case, so that $|C|$ is bounded by $|B/4|$ and can be considerably smaller.

Teleseismic P-coda reverberations with periods $T \gtrsim 1$ sec are typically used to investigate the properties of the bulk crust, e.g., its Poisson ratio, or differences between upper and lower crustal layers. Given the above estimates, our choice to neglect the $\cos 4\xi$ azimuthal variation in P velocity seems reasonable as a working hypothesis for the bulk of the crust. However, shallow structures, such as sedimentary basins, may require this parameter for an accurate description of the P-coda.

REFERENCES

AGUE, J. J. (1995), *Deep Crustal Growth of Quartz, Kyanite and Garnet into Large Aperture, Fluid-filled Fractures, Northeastern Connecticut, USA*, J. Metam. Geol. *13*, 299–314.

ANDERSON, D. L., *A Theory of the Earth* (Blackwell Scientific, Oxford 1989).

BABUSKA, V., and PROS, Z. (1984), *Velocity Anisotropy in Granodiorite and Quartzite due to the Distribution of Microcracks*, Geophys. J. Roy. Astron. Soc. *76*, 121–127.

BABUSKA, V., and CARA, M., *Seismic Anisotropy in the Earth* (Kluwer Academic, Dordrecht 1991).

BABUSKA, V., PLOMEROVA, J., and SILENY, J. (1993), *Models of Seismic Anisotropy in the Deep Continental Lithosphere*, Phys. Earth and Planet. Int. *78*, 167–191.

BACKUS, G. E. (1962), *Long-wave Elastic Anisotropy Produced by Horizontal Layering*, J. Geophys. Res. *67*, 4427–4440.

BACKUS, G. E. (1965), *Possible Forms of Seismic Anisotropy of the Uppermost Mantle under Oceans*, J. Geophys. Res. *70*, 3429–3439.

BLACKMAN, D. K., KENDALL, J.-M., DAWSON, P. R., WENK, H.-R., BOYCE, D., and JASON PHIPPS MORGAN (1996), *Teleseismic Imaging of Subaxial Flow at Mid-ocean Ridges: Travel-time Effects of Anisotropic Mineral Texture in the Mantle*, Geophys. J. Int. *127*, 415–426.

BURLINI, L., and FOUNTAIN, D. M. (1993), *Seismic Anisotropy of Metapelites from the Ivrea-Verbano Zone and Serie dei Leghi (Northern Italy)*, Phys. Earth and Planet. Int. *78*, 301–317.

CHRISTENSEN, N. I. (1996), *Poisson's Ratio and Crustal Seismology*, J. Geophys. Res. *101*, 3139–3156.

CRAMPIN, S. (1984), *Effective Elastic Constants for Wave Propagation through Cracked Solids*, Geophys. J. Roy. Astron. Soc. *76*, 135–145.

CRAMPIN, S. (1991), *Wave Propagation Through Fluid-filled Inclusions of Various Shapes: Interpretation of Extensive-dilatancy Anisotropy*, Geophys. J. Int. *104*, 611–623.

COLEMAN, M. (1996), *Orogen-parallel and Orogen-perpendicular Extension in the Central Nepalese Himalayas*, GSA Bulletin *108*, 1594–1607.

FARRA, V., VINNIK, L. P., ROMANOWICZ, B., KOSAREV, G. L., and KIND, R. (1991), *Inversion of Teleseismic S Particle Motion for Azimuthal Anisotropy in the Upper Mantle; A Feasibility Study*, Geophys. J. Int. *106*, 421–431.

FRYER, G. J., and FRAZER, L. N. (1987), *Seismic Waves in Stratified Anisotropic Media—II. Elastodynamic Eigensolutions for Some Anisotropic Systems*, Geophys. J. Roy. Astron. Soc. *91*, 73–102.

GAHERTY, J. B., and JORDAN, T. H. (1995), *Lehmann Discontinuity as the Base of an Anisotropic Layer Beneath Continents*, Science *268*, 1468–1471.

GARMANY, J. (1983), *Some Properties of Elastodynamic Eigensolutions in Stratified Media*, Geophys. J. Roy. Astron. Soc. *75*, 565–570.

GRESILLAUD, A., and CARA, M. (1996), *Anisotropy and P-wave Tomography; A New Approach for Inverting Teleseismic Data from a Dense Array of Stations*, Geophys. J. Int. *126*, 77–91.

HEARN, T. M. (1996), *Anisotropic P_n Tomography in the Western United States*, J. Geophys. Res. *101*, 8403–8414.

HELBIG, K., *Foundations of Anisotropy for Exploration Seismics* (Pergamon/Elsevier Science, Oxford 1994).

HU, G. (1993), *Lower Crustal and Moho Structures beneath Beijing, China Determined by Formal Inversion of Single Station Measurements of Teleseismic P-wave Polarization Anomalies*, EOS *74*, 426.

HUDSON, J. A. (1981), *Wave Speeds and Attenuation of Elastic Waves in Material Containing Cracks*, Geophys. J. Roy. Astron. Soc. *64*, 133–150.

KENNETT, B. L. N., *Seismic Wave Propagation in Stratified Media* (Cambridge University Press, Cambridge 1983).

KERN, H., WALTHER, Ch., FLUH, E. R., and MARKER, M. (1993), *Seismic Properties of Rocks Exposed in the POLAR Profile Region—Constraints on the Interpretation of the Refraction Data*. Precambrian Research *64*, 169–187.

KOSAREV, G. L., MAKEYEVA, L. I., and VINNIK, L. P. (1984), *Anisotropy of the Mantle Inferred from Observations of P to S Converted Waves*, Geophys. J. Roy. Astron. Soc *76*, 209–220.

LANGSTON, C. A. (1977), *The Effect of Planar Dipping Structure on Source and Receiver Responses for Constant Ray Parameter*, Bull. Seismol. Soc. Am. *67*, 1029–1050.

LEVIN, V., MENKE, W., and LERNER-LAM, A. L. (1996), *Seismic Anisotropy in Northeastern U.S. as a Source of Significant Teleseismic P Travel-time Anomalies*, Geophys. J. Int. *126*, 593–603.

LEVIN, V., and PARK, J. (1977a), *Anisotropy in the Ural Mountains Foredeep from Teleseismic Receiver Functions*, Geophys. Res. Letts. *24*, 1283–1286.

LEVIN, V., and PARK, J. (1977b), *P-SH Conversions in a Flat-layered Medium with Anisotropy of Arbitrary Orientation*, Geophys. J. Int., in press.

LYNN, H. B. (1991), *Field Measurements of Azimuthal Anisotropy: First 60 Meters, San Francisco Bay Area, CA, and Estimation of the Horizontal Stress Ratio from V_{S1}/V_{S2}*, Geophysics *56*, 822–832.

MAINPRICE, D., and SILVER, P. G. (1993), *Constraints on the Interpretation of Teleseismic SKS Observations from Kimberlite Nodules from the Subcontinental Mantle*, Phys. Earth and Planet. Int. *78*, 257–280.

NICOLAS, A., BOUDIER, F., and BOULIER, A. M. (1973), *Mechanism of Flow in Naturally and Experimentally Deformed Periodotites*, Am. J. Sci. *10*, 853–876.

OWENS, T. J., and CROSSON, R. S. (1988), *Shallow Structure Effects on Broad-band Teleseismic P Waveforms*, Bull. Seismol. Soc. Am. *77*, 96–108.

PARK, J. (1993), *The Sensitivity of Seismic Free Oscillations to Upper Mantle Anisotropy I. Zonal Structure*, J. Geophys. Res. *98*, 19933–19949.

PARK, J. (1996), *Surface Waves in Layered Anisotropic Structures*, Geophys. J. Int. *126*, 173–183.

RAITT, R. W., SHOR Jr., G. G., FRANCIS, T. J. G., and MORRIS, G. B. (1969), *Anisotropy of the Pacific Upper Mantle*, J. Geophys. Res. *74*, 3095–3109.

RIBE, N. (1992), *On the Relation Between Seismic Anisotropy and Finite Strain*, J. Geophys. Res. *97*, 8737–8747.

SHEARER, P. M., and ORCUTT, J. A. (1986), *Compressional and Shear-wave Anisotropy in the Oceanic Lithosphere—the Ngendie Seismic Refraction Experiment*, Geophys. J. Roy. Astron. Soc. *87*, 967–1003.

SILVER, P. G. (1996), *Seismic Anisotropy Beneath the Continents: Probing the Depths of Geology*, Ann. Rev. Earth Planet. Sci. *24*, 385–432.

SILVER, P. G., and CHAN, W. W. (1991), *Shear-wave Splitting and Subcontinental Mantle Deformation*, J. Geophys. Res. *96*, 16429–16454.

THOMSEN, L. (1986), *Weak Elastic Anisotropy*, Geophysics *51*, 1954–1966.

VINNIK, L. P., MAKEYEVA, L. I., MILEV, A., and USENKO, A. Yu. (1992), *Global Patterns of Azimuthal Anisotropy and Deformations in the Continental Mantle*, Geophys. J. Int. *111*, 433–447.

VINNIK, L. P., and MONTAGNER, J.-P. (1996), *Shear-wave Splitting in the Mantle Ps Phases*, Geophys. Res. Letts. *23*, 2449–2452.

VISSER, J., and PAULLSEN, H. (1993), *The Crustal Structure from Teleseismic P-wave Coda—II. Application to Data of the NARS Array in Western Europe and Comparison with Deep Seismic Sounding Data*, Geophys. J. Int. *112*, 26–38.

WESSEL, P., and SMITH, W. H. F. (1991), *Free Software Helps Map and Display Data*, EOS Trans. AGU *72*, 441.

YU, Y., and PARK, J. (1933), *Upper Mantle Anisotropy and Coupled-mode Long-period Surface Waves*, Geophys. J. Int. *114*, 473–489.

ZANDT, G., and AMMON, C. J. (1995), *Continental Crust Composition Constrained by Measurements of Crustal Poisson's Ratio*, Nature *374*, 152–154.

ZHANG, S., and KARATO, S. (1995), *Lattice Preferred Orientation of Olivine Aggregates Deformed in Simple Shear*, Nature *375*, 774–777.

ZHI, Z., and SCHWARTZ, S. Y. (1994), *Seismic Anisotropy in the Shallow Crust of the Loma Prieta Segment of the San Andreas Fault System*, J. Geophys, Res. *99*, 9651–9661.

ZHU, L., OWENS, T. J., and RANDALL, G. E. (1995), *Lateral Variation in Crustal Structure of the Northern Tibetan Plateau Inferred from Teleseismic Receiver Functions*, Bull. Seismol. Soc. Am. *85*, 1531–1540.